Available online at www.sciencedirect.com
SCIENCE DIRECT®
Journal of Sound and Vibration 285 (2005) 1071–1091
JOURNAL OF SOUND AND VIBRATION
www.elsevier.com/locate/jsvi

Vibration and instability of functionally graded circular cylindrical spinning thin-walled beams

Sang-Yong Oh[a], Liviu Librescu[a,*], Ohseop Song[b]

[a]*Engineering Science and Mechanics Department, Virginia Polytechnic Institute and State University, Blacksburg, VA 24061-0219, USA*
[b]*Chungnam National University, Daejon City 305-764, Republic of Korea*

Received 10 November 2003; received in revised form 2 September 2004; accepted 14 September 2004
Available online 25 December 2004

Abstract

Problems related to the thermoelastic modeling and behavior of circular cylindrical thin-walled beams made of functionally graded materials and spinning with a constant speed about their longitudinal axis are addressed. In this context, the implications of conservative and gyroscopic forces considered in conjunction with a temperature field that yields the material degradation of the beam elastic properties, on their vibration and instability are investigated. A continuously graded variation in composition of the ceramic and metal phases across the beam wall thickness in terms of a simple power law distribution is implemented. Results highlighting the effects of the volume fraction, temperature gradient (considered in conjunction with the temperature degradation of material properties), compressive axial load and rotational speed on vibration and instability of spinning beams are presented and pertinent conclusions are drawn.

1. Introduction

Thin-walled structural systems spinning about their longitudinal axis are used in the most diverse areas of modern technology. In this sense, these are used as a shaft, for power transmission in aeropropulsion systems, in helicopter drive applications, and in industrial

*Corresponding author. Tel.: +1 540 231 5916; fax: +1 540 231 4574.
E-mail address: librescu@vt.edu (L. Librescu).

0022-460X/$ - see front matter © 2004 Elsevier Ltd. All rights reserved.
doi:10.1016/j.jsv.2004.09.018

machines such as steam and gas turbines. In addition, these are used in the cutting tools used in boring and milling operations. Moreover, the axial booms attached to spin-stabilized spacecraft and subjected to solar heating, belong to the category of structural systems considered in this paper.

In order to enhance their vibrational behavior, eliminate or even postpone the occurrence of any instability jeopardizing their operational life and expand their efficiency, a better understanding of their behavior is required. In addition, having in view that these structural systems operate in severe environmental conditions such as high temperatures, in order to resist without catastrophic failures, advanced structural models have to be devised.

In this context, the application of the functionally gradient material (FGM) concept is likely to eliminate the shortcomings that are inherently generated when instead, standard composite material structures are used.

The FGMs are special composites, microscopically inhomogeneous whose thermomechanical properties vary smoothly and continuously in pre-determined directions throughout the body of the structure. Herein, this feature is achievable by varying the volume fraction of constituent phases in the thickness direction, that usually are from ceramic and metal.

The ceramic in a FGM offers thermal barrier effects and protects the metal from corrosion and oxidation, whereas the FGM is toughened and strengthened by the metallic composition. As a result, these materials are able to withstand high-temperature gradients, without structural failure. Such features are vital, specially in aeronautical and space applications, where contradictory functions, such as refractoriness and chemical inertness with toughness should be met.

In contrast to standard laminated composite structures, whose material properties are piecewise constant through their thickness, and as a result, are exposed to adverse interface effects that can yield failure of the structure, in the case of the FGMs, due to the continuous variation of their material properties, such effects are precluded to occur.

In addition to the research work devoted to modeling of the three-dimensional (3-D) FGM media, the studies involving thin-walled structures made of FGMs have been mainly devoted to beams, plates, and shells. For an exhaustive, but far from complete list of references on the research work accomplished in this area, see Ref. [1]. To the best of the authors' knowledge, in spite of its evident practical importance, no research work related to the modeling and behavior of spinning circular cylindrical thin-walled beams operating in a high-temperature environment and made of FGMs has been yet accomplished. This paper is devoted to this topic.

Herein, the case of a straight, circular cylindrical thin-walled beam spinning with a constant angular velocity about its longitudinal axis and exposed to a steady temperature field experiencing a gradient through the wall thickness is considered. It is assumed that the beam is made of FGMs whose properties vary continuously across the wall thickness and that the material properties are temperature dependent. In this context, the modeling, the vibrational and instability behavior of circular cylindrical beams spinning about their longitudinal axis are investigated, and the effect of material degradation due to the temperature field is highlighted. This paper represents an extension of a number of previous results obtained in the context of composite structures in Refs. [2,3].

2. Structural model

2.1. Coordinate systems and basic assumptions

The case of a straight flexible circular cylindrical beam of length L spinning about its longitudinal z-axis at a constant rate Ω and subjected to the longitudinal compressive dead force P is considered (see Fig. 1). Two coordinate systems, an inertial one, $OXYZ$, and a body attached rotating frame of reference $Oxyz$, with their common origin O at the geometric center (coinciding with the elastic center of the beam), are considered. It is supposed that the axes of the two coordinate systems coincide only when $t = 0$ while, in the underformed configuration, the body-fixed and inertial coordinates Oz and OZ coincide at any time t. Associated with the coordinate systems (x, y, z) and (X, Y, Z), one define the unit vectors $(\mathbf{i}, \mathbf{j}, \mathbf{k})$ and $(\mathbf{I}, \mathbf{J}, \mathbf{K})$, respectively (see Fig. 2). In addition to the previously defined coordinate systems, a local (surface) one, (n, s, z), associated with the thin-walled beam, is considered, where n is the thickness coordinate $(-h/2 \leqslant n \leqslant h/2)$, while s and z stand for circumferential and the spanwise coordinates, respectively (see Figs. 1 and 2). As a result of the stipulated assumptions one can represent the spin rate vector as $\mathbf{\Omega} = \Omega\mathbf{k}(\equiv \Omega\mathbf{K})$ and $\dot{\mathbf{\Omega}} = 0$.

Herein, the case of a single-cell thin-walled beam of circular cross-sectional shape is considered. Toward its modeling, the following assumptions are adopted: (1) the original cross section of the beam is preserved in the sense that no distortions in the plane of the cross section occur; (2) transverse shear effects are incorporated; (3) a pointwise variation of material properties of the two constituent phases, i.e. ceramic and metal across the beam thickness is featured; and (4), the study is confined to only the coupled transversal–lateral bending that is decoupled from the twist and extension motions.

2.2. Kinematics

In light of the previously mentioned assumptions, in order to reduce the 3-D elasticity problem to an equivalent 1-D one, the components of the displacement vector are obtained by specializing

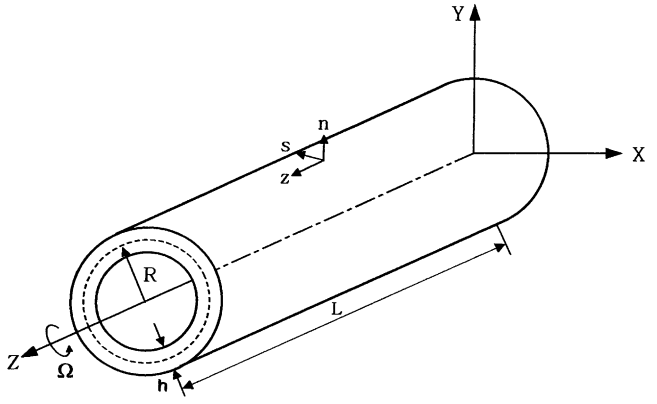

Fig. 1. Geometry of the thin-walled beam of circular cross section.

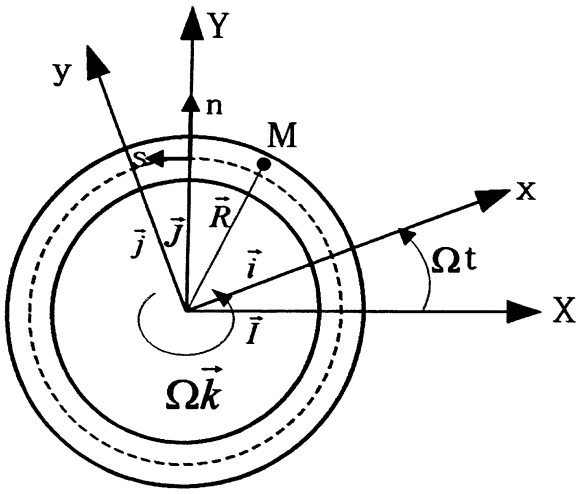

Fig. 2. Inertial (X, Y, Z) and body fixed (x, y, z) coordinate systems.

for the problem at hand the ones from Ref. [4]:

$$u(x, y, z; t) = u_0(z; t), \quad v(x, y, z; t) = v_0(z; t), \tag{1a,b}$$

$$w(x, y, z; t) = \theta_x(z; t)\left[y(s) - n\,\frac{\mathrm{d}x}{\mathrm{d}s}\right] + \theta_y(z; t)\left[x(s) + n\,\frac{\mathrm{d}y}{\mathrm{d}s}\right]. \tag{1c}$$

In these equations $u_0(z; t)$ and $v_0(z; t)$ denote the rigid body translations along the x- and y-axis, while $\theta_x(z; t)$, $\theta_y(z, t)$ denote the rotations about the x- and y-axis, respectively. The expressions of θ_x and θ_y are

$$\theta_x(z; t) = \gamma_{yz}(z; t) - v_0'(z; t), \quad \theta_y(z; t) = \gamma_{xz}(z; t) - u_0'(z; t). \tag{2a,b}$$

From Eqs. (2) it is seen that in the absence of transverse shear effects:

$$\theta_x(z; t) = -v_0'(z; t), \quad \theta_y(z; t) = u_0'(z; t). \tag{3a,b}$$

In these equations, as well as in those that follow, primes denote differentiation with respect to the longitudinal z coordinate.

For further use, additional kinematic quantities are indicated here. Among these, the position vector of a generic point $M(x, y, z)$ belonging to the deformed structure is

$$\mathbf{R}(x, y, z; t) = (x + u)\mathbf{i} + (y + v)\mathbf{j} + (z + w)\mathbf{k}, \tag{4}$$

where x, y and z are the Cartesian coordinates of the points of the continuum in its undeformed state. Recalling that the spin rate was assumed to be constant, and using the expressions for the time derivatives of unit vectors, the velocity and acceleration of a generic point are

$$\dot{\mathbf{R}} = [\dot{u} - \Omega(y + v)]\mathbf{i} + [\dot{v} + \Omega(x + u)]\mathbf{j} + \dot{w}\mathbf{k}, \tag{5a}$$

$$\ddot{\mathbf{R}} = [\ddot{u} - 2\Omega\dot{v} - (x + u)\Omega^2]\mathbf{i} + [\ddot{v} + 2\Omega\dot{u} - (y + v)\Omega^2]\mathbf{j} + \ddot{w}\mathbf{k}. \tag{5b}$$

In these equations the superposed dots denote derivatives with respect to time t.

Based on the displacement representations (1) and (2), in the framework of purely bending motions, the strain measures assume the form:

Axial strain:

$$\varepsilon_{zz}(n,s,z,t) = \bar{\varepsilon}_{zz}(s,z,t) + n\bar{\bar{\varepsilon}}_{zz}(s,z,t), \tag{6a}$$

where

$$\bar{\varepsilon}_{zz}(s,z,t) = \theta'_x(z,t)y(s,z) + \theta'_y(z,t)x(s,z) \tag{7a}$$

and

$$\bar{\bar{\varepsilon}}_{zz}(s,z,t) = \theta'_y(z,t)\frac{\mathrm{d}y}{\mathrm{d}s} - \theta'_x(z,t)\frac{\mathrm{d}x}{\mathrm{d}s}, \tag{7b}$$

are the axial strains associated with the primary and secondary warping, respectively.

Tangential shear strain:

$$\varepsilon_{sz}(n,s,z,t) \equiv \bar{\varepsilon}_{sz}(s,z,t), \tag{8}$$

where

$$\bar{\varepsilon}_{sz}(s,z,t) = [\theta_y(z,t) + u'_0(z,t)]\frac{\mathrm{d}x}{\mathrm{d}s} + [\theta_x(z,t) + v'_0(z,t)]\frac{\mathrm{d}y}{\mathrm{d}s}. \tag{9}$$

Transverse shear strain:

$$\varepsilon_{nz}(s,z,t) = [\theta_y(z,t) + u'_0(z,t)]\frac{\mathrm{d}y}{\mathrm{d}s} - [\theta_x(z,t) + v'_0(z,t)]\frac{\mathrm{d}x}{\mathrm{d}s}. \tag{10}$$

2.3. Constitutive equations for functionally graded beams

The design of high-performance spinning structures must meet high efficiency and high reliability, regardless of the severe temperature gradients under which these may operate. In order to address these demands, functionally graded ceramic–metal based materials are used. These materials are isotropic but, due to the fact that the shaft wall can be rather thick, in order to accomodate this feature, transverse shear effects will be incorporated.

As a result, the thermoelastic constitutive law adapted in this case of thin-walled structures is expressed as

$$\begin{bmatrix} \sigma_{ss} \\ \sigma_{zz} \\ \sigma_{zn} \\ \sigma_{ns} \\ \sigma_{sz} \end{bmatrix} = \begin{bmatrix} Q_{11} & Q_{12} & 0 & 0 & 0 \\ Q_{12} & Q_{11} & 0 & 0 & 0 \\ 0 & 0 & Q_{44} & 0 & 0 \\ 0 & 0 & 0 & Q_{55} & 0 \\ 0 & 0 & 0 & 0 & Q_{66} \end{bmatrix} \begin{bmatrix} \varepsilon_{ss} \\ \varepsilon_{zz} \\ \varepsilon_{zn} \\ \varepsilon_{ns} \\ \varepsilon_{sz} \end{bmatrix} - \begin{bmatrix} \hat{\alpha}\Delta T \\ \hat{\alpha}\Delta T \\ 0 \\ 0 \\ 0 \end{bmatrix}. \tag{11}$$

Herein, the reduced thermoelastic coefficients are defined as

$$Q_{11} = \frac{E}{1-v^2}, \quad Q_{12} = \frac{Ev}{1-v^2}, \quad Q_{66} = \frac{E}{2(1+v)} (\equiv G), \quad Q_{44} = Q_{55} = k^2 G,$$
$$\hat{\alpha} = \frac{E}{1-v}\,\alpha, \tag{12a–e}$$

where E and v are the Young's modulus and Poisson's ratio, respectively, k^2 is the transverse shear correction factor, $\Delta T(s,z,n)$ is the steady-state temperature rise from that of the stress free state, while α is the thermal expansion coefficient. Although assumed to be large, the temperature rise cannot be however too extreme, as not to trigger, for the metallic constituent, elastoplastic or viscoelastic responses.

For a model of ceramic/metal FGM, in the case of a uniform wall thickness whose reference surface is at $n = 0$, we assume that the material properties vary continuously across the blade thickness according to the power law distribution [5]:

$$E(n) = (E_c - E_m)\left(\frac{2n+h}{2h}\right)^K + E_m, \quad v(n) = (v_c - v_m)\left(\frac{2n+h}{2h}\right)^K + v_m,$$

$$\rho(n) = (\rho_c - \rho_m)\left(\frac{2n+h}{2h}\right)^K + \rho_m, \quad \alpha(n) = (\alpha_c - \alpha_m)\left(\frac{2n+h}{2h}\right)^K + \alpha_m, \tag{13a–d}$$

where subscripts m and c identify the properties affiliated to metal and ceramic, respectively.

In Eqs. (13), K ($0 \leqslant K \leqslant \infty$) is the power law exponent. From Eqs. (13) it results that for $n = h/2$, $E \to E_c$, $v \to v_c$ and $\rho \to \rho_c$, while for $n = -h/2$, $E \to E_m$, $v \to v_m$ and $\rho \to \rho_m$.

This shows that consistent with this law, the material properties vary continuously from the top surface of the beam where the material is entirely ceramic, to fully metal at the bottom surface. From Eqs. (13) it becomes also evident that, starting with $K = 0$, for which the beam is entirely of ceramic, the increase of the volume fraction parameter K implies a continuous increase of the metal content to the detriment of the ceramic.

It is assumed that the blade is subjected to a steady-state 1-D temperature distribution through its wall thickness, $T = T(n)$. The temperatures at $n = \pm h/2$ are $T(n = h/2) \equiv T_t$ and $T(n = -h/2) = T_b$, where T_t and T_b denote the temperatures at the top and bottom surfaces of the FGM beam, respectively.

The temperature distribution in the thickness direction fulfilling the conditions on the bounding surfaces yields the steady-state temperature distribution $T(n)$,

$$T(n) = T_b \left[1 + \frac{\lambda}{\int_{-h/2}^{h/2} \frac{1}{\kappa(n)}\,\mathrm{d}n} \int_{-h/2}^{n} \frac{\mathrm{d}n}{\kappa(n)}\right], \tag{14a}$$

where

$$\lambda = \frac{T_t - T_b}{T_b} \tag{15}$$

represents a measure of the normalized temperature gradient across the beam wall thickness, where $\kappa(n)$ is the thermal conductivity. Throughout the numerical simulations, it will be considered $T_b = 300\,\mathrm{K}$.

As concerns the thermal conductivity $\kappa(n)$ of the FGM, it is assumed to vary according to the law

$$\kappa(n) = (\kappa_c - \kappa_m)\left(\frac{2n+h}{2h}\right)^K + \kappa_m \tag{16}$$

and that the thermal conductivities κ_c and κ_m are temperature-independent. With the exception of this restriction, the remaining properties of the FGM are temperature dependent, and vary according to the law obtained from experiments. These are expressed in a generic form as [5]

$$P(n) = P_0(P_{-1}/T + 1 + P_1 T + P_2 T^2 + P_3 T^3). \tag{17}$$

Herein, P_0, P_{-1}, P_1, P_2 and P_3 are the constants in the cubic fit of the specific temperature-dependent material property, where T (in Kelvin) is the environmental temperature. For the constituents phases of silicon nitride (SN) and stainless steele (SS), the constants P_i are supplied e.g. in Ref. [5]. For the sake of completeness their values are supplied in Table 1.

As an alternative procedure, the Mori–Tanaka mean field scheme can be applied to evaluate the locally effective material properties (see Ref. [6]).

Consistent with the present case, the 1-D constitutive equations determined in conjunction with Eqs. (11) and (13) are

$$\begin{bmatrix} M_y \\ M_x \\ Q_x \\ Q_y \end{bmatrix} = \begin{bmatrix} a_{22} & 0 & 0 & 0 \\ 0 & a_{33} & 0 & 0 \\ 0 & 0 & a_{44} & 0 \\ 0 & 0 & 0 & a_{55} \end{bmatrix} \begin{bmatrix} \theta'_y \\ \theta'_x \\ u'_0 + \theta_y \\ v'_0 + \theta_x \end{bmatrix} + \begin{bmatrix} M_y^{\mathrm{T}} \\ M_x^{\mathrm{T}} \\ 0 \\ 0 \end{bmatrix}. \tag{18}$$

In these equations, $a_{ij}(= a_{ji})$ are stiffness coefficients while M_y^{T} and M_x^{T} are 1-D thermal moment terms. In addition, (Q_x and Q_y) denote the 1-D shear forces in the x- and y-directions,

Table 1
Material properties of FGM constituents

Material properties	Materials	P_0	P_{-1}	P_1	P_2	P_3
	SN	348.43×10^9	0	-3070×10^{-4}	2.160×10^{-7}	-8946×10^{-11}
$E\,(\mathrm{N/m^2})$						
	S-S	201.04×10^9	0	3.079×10^{-4}	-6.534×10^{-7}	0
	SN	0.2400	0	0	0	0
v						
	S-S	0.3262	0	-2.002×10^{-4}	3.797×10^{-7}	0
	S-N	2370	0	0	0	0
$\rho\,(\mathrm{kg/m^3})$						
	S-S	8166	0	0	0	0

The properties are evaluated at $T = 300\,\mathrm{K}$.

respectively, and (M_x, M_y) are the 1-D stress couples about the x- and y-axis, respectively. Their expressions are displayed in Appendix A.

2.4. Equations of motion and boundary conditions

To derive the equations of motion of functionally graded circular cylindrical spinning shaft and the associated boundary conditions, the extended Hamilton's principle is used. This can be formulated as

$$\int_{t_1}^{t_2} (\delta \mathbb{K} - \delta V + \delta W)\,\mathrm{d}t = 0, \tag{19}$$

$$\delta u_0 = \delta v_0 = \delta \theta_x = \delta \theta_y = 0 \quad \text{at } t = t_1, t_2,$$

where $\mathbb{K}$ and V are the kinetic and strain energy, respectively, δW is the virtual work of external forces, t_1 and t_2 are two arbitrary instants of time, and δ is the variation operator. In this context

$$\begin{aligned}
&\int_{t_1}^{t_2} \delta \mathbb{K}\,\mathrm{d}t \left(\equiv -\int_{t_1}^{t_2} \mathrm{d}t \int_{\tau} \rho \ddot{\mathbf{R}} \cdot \delta \mathbf{R}\,\mathrm{d}\tau \right) \\
&\quad = -\int_{t_1}^{t_2} \mathrm{d}t \int_{\tau} \{[\ddot{u} - 2\Omega\dot{v} - \Omega^2(x+u)]\delta u + [\ddot{v} + 2\Omega\dot{u} - (y+v)\Omega^2]\delta v + \ddot{w}\delta w\}\rho\,\mathrm{d}\tau \\
&\quad = -\int_{t_1}^{t_2} \left\{ \left[\ddot{u}_0 - 2\Omega\dot{v}_0 - \Omega^2(x+u_0)\right]\delta u_0 + [\ddot{v}_0 + 2\Omega\dot{u}_0 - (y+v_0)\Omega^2]\delta v_0 \right. \\
&\qquad \left. + \left[\left(y - n\frac{\mathrm{d}x}{\mathrm{d}s} \right)\ddot{\theta}_x + \left(x + n\frac{\mathrm{d}y}{\mathrm{d}s} \right)\ddot{\theta}_y \right] \delta \left[\theta_x \left(y - n\frac{\mathrm{d}x}{\mathrm{d}s} \right) + \theta_y \left(x + n\frac{\mathrm{d}y}{\mathrm{d}s} \right) \right] \right\} \mathrm{d}\tau.
\end{aligned} \tag{20}$$

In this equation $\mathrm{d}\tau (\equiv \mathrm{d}s\,\mathrm{d}n\,\mathrm{d}z)$ and ρ denote the differential volume element and the material mass density, respectively. For the variation of the strain energy δV one obtains (see Refs. [2,3])

$$\begin{aligned}
\int_{t_1}^{t_2} \int_{\tau} \sigma_{ij}\delta\varepsilon_{ij}\,\mathrm{d}\tau\,\mathrm{d}t = \int_{t_1}^{t_2} \int_{0}^{L} &-\{(M_y' - Q_x)\delta\theta_y + (M_x' - Q_y)\delta\theta_x + [Q_x' + (T_z u_0')']\delta u_0 \\
&+ [Q_y' + (T_x v_0')']\delta v_0\}\,\mathrm{d}z\,\mathrm{d}t + \int_{t_1}^{t_2} [M_y\delta\theta_y + M_x\delta\theta_x \\
&+ (Q_x + T_z u_0')\delta u_0 + (Q_y + T_z v_0')\delta v_0]_0^L\,\mathrm{d}t.
\end{aligned} \tag{21}$$

These equations are supplied in terms of 1-D stress-resultants (T_x, Q_x and Q_y) that denote the axial and the shear forces in the x- and y-directions, respectively, and stress couples (M_x, M_y) about the x- and y-axis, respectively. Their expressions are

$$T_z(z,t) = \oint N_{zz}\,\mathrm{d}s, \quad M_y(z,t) = \oint \left(xN_{zz} + L_{zz}\frac{\mathrm{d}y}{\mathrm{d}s} \right)\mathrm{d}s,$$

$$M_x(z,t) = \oint \left(yN_{zz} - L_{zz}\frac{\mathrm{d}x}{\mathrm{d}s} \right)\mathrm{d}s, \quad Q_x(z,t) = \oint \left(N_{sz}\frac{\mathrm{d}x}{\mathrm{d}s} + L_{zn}\frac{\mathrm{d}y}{\mathrm{d}s} \right)\mathrm{d}s,$$

$$Q_y(z,t) = \oint \left(N_{sz}\frac{\mathrm{d}y}{\mathrm{d}s} - L_{zn}\frac{\mathrm{d}x}{\mathrm{d}s} \right)\mathrm{d}s. \tag{22a–e}$$

As concerns the virtual work of external forces, its expression is

$$\delta W = \int_0^L [p_x \delta u_0 + p_y \delta v_0 + m_x \delta\theta_x + m_y \delta\theta_y]\,\mathrm{d}s + [\underset{\sim}{Q}_x\,\delta u_0 + \underset{\sim}{Q}_y\,\delta v_0 + \underset{\sim}{M}_x\,\delta\theta_x + \underset{\sim}{M}_y\,\delta\theta_y]|_0^L, \tag{23}$$

where p_x and p_y are the distributed loads, m_x and m_y are the distributed moments about the axes x and y, respectively, while the quantities underscored by a tilde denote prescribed quantities. Using Eqs. (20)–(23) in Hamilton's principle, invoking the stationarity of the functional in the time interval $[t_1, t_2]$ and the fact that the variations $(\delta u_0, \delta v_0, \delta\theta_x, \delta\theta_y)$ are independent and arbitrary, their coefficients in the integrands must vanish independently. This yields the equations of motion and the boundary conditions.

As a result, from Eq. (19), there are obtained the governing equations involving the transversal bending (flapping)-lateral bending (lagging)- transverse shear coupling. In addition, with the effect of a longitudinal dead force P positive in compression, the governing equations read

$$\delta u_0 : a_{44}(u_0' + \theta_y)' - P u_0'' + p_x(z,t) = b_1 \ddot{u}_0 - \underline{2 b_1 \Omega \dot{v}_0} - b_1 u_0 \Omega^2,$$

$$\delta v_0 : a_{55}(v_0' + \theta_x)' - P v_0'' + p_y(z,t) = b_1 \ddot{v}_0 + \underline{2 b_1 \Omega \dot{u}_0} - b_1 v_0 \Omega^2,$$

$$\delta\theta_y : a_{22}\theta_y'' - a_{44}(u_0' + \theta_y) + m_y(z,t) = \underline{(b_5 + \delta_n b_{15})\ddot{\theta}_y} + (M_y^{\mathrm{T}})',$$

$$\delta\theta_x : a_{33}\theta_x'' - a_{55}(v_0' + \theta_x) + m_x(z,t) = \underline{(b_4 + \delta_n b_{14})\ddot{\theta}_x} + (M_x^{\mathrm{T}})' \tag{24a–d}$$

and the *boundary conditions* at $z = 0, L$:

$$\delta u_0 : Q_x = \underset{\sim}{Q}_x \quad \text{or} \quad u_0 = \underset{\sim}{u}_0,$$

$$\delta v_0 : Q_y = \underset{\sim}{Q}_y \quad \text{or} \quad v_0 = \underset{\sim}{v}_0,$$

$$\delta\theta_y : M_y = \underset{\sim}{M}_y \quad \text{or} \quad \theta_y = \underset{\sim}{\theta}_y,$$

$$\delta\theta_x : M_x = M\sim_x \quad \text{or} \quad \theta_x = \underset{\sim}{\theta}_x. \tag{25a–d}$$

In terms of displacement quantities, the static version of homogeneous boundary conditions becomes

$$\delta u_0 : a_{44}(u_0' + \theta_y) - P u_0' = 0,$$

$$\delta v_0 : a_{55}(v_0' + \theta_x) - P v_0' = 0,$$

$$\delta\theta_y : a_{22}\theta_y' = M_y^{\mathrm{T}},$$

$$\delta\theta_x : a_{33}\theta_x' = M_x^{\mathrm{T}}. \tag{26a–d}$$

The coefficients b_i appearing in these equations as well as in the forthcoming ones denote reduced mass terms, while δ_n is a tracer that takes the values 1 or 0, depending on whether the effects off the mid-line contour are taken into consideration, or discarded, respectively. The expression of b_i are provided in Appendix A. The system of governing equations reveals a coupling among the transversal bending, the lateral bending and the transverse shear effects. As it clearly appears, the coupling between the transversal and lateral bending is due to only the Coriolis effect. Its terms are associated with the gyroscopic effect and are underscored by a dotted line. The terms underscored by a solid line are associated with the rotatory inertias.

3. Euler–Bernonulli counterpart of the governing equations

The classical version of the governing equations and of boundary conditions can be obtained by exactly eliminating the $a_{44}(u_0' + \theta_y)$ and $a_{55}(v_0' + \theta_x)$ terms among Eqs. (24) and (26), and considering afterwards $\theta_y \to -u_0'$ and $\theta_x \to -v_0'$. This way we obtain the following governing equations:

$$\begin{aligned}
&\delta u_0 : a_{22}u_0'''' + Pu_0'' - p_x - m_y' + b_1(\ddot{u}_0 - \Omega^2 u_0) - \underline{2b_1\Omega\dot{v}_0} - \underline{(b_5 + \delta_n b_{15})\ddot{u}_0''} \\
&\quad + (M_y^{\mathrm{T}})'' = 0, \\
&\delta v_0 : a_{33}v_0'''' + Pv_0'' - p_y - m_x' + b_1(\ddot{v}_0 - \Omega^2 v_0) + \underline{2b_1\Omega\dot{u}_0} - \underline{(b_4 + \delta_n b_{14})\ddot{v}_0''} \\
&\quad + (M_x^{\mathrm{T}})'' = 0.
\end{aligned} \tag{27a, b}$$

As concerns the classical *homogeneous* counterpart of the boundary conditions, these are:

$$\begin{aligned}
&\delta u_0 : M_y' = 0; \quad \text{or} \quad u_0 = 0, \\
&\delta v_0 : M_x' = 0; \quad \text{or} \quad v_0 = 0, \\
&\delta u_0' : M_y = 0; \quad \text{or} \quad u_0' = 0, \\
&\delta v_0' : M_x = 0; \quad \text{or} \quad v_0' = 0.
\end{aligned} \tag{28a–d}$$

In terms of displacement quantities, the static boundary conditions are:

$$\begin{aligned}
&\delta v_0 : a_{33}v_0''' + Pv_0' - \underline{(b_4 + \delta_n b_{14})\ddot{v}_0'} + (M_x^{\mathrm{T}})' - m_x = 0, \\
&\delta u_0 : a_{22}u_0''' + Pu_0' - \underline{(b_5 + \delta_n b_{15})\ddot{u}_0'} + (M_y^{\mathrm{T}})' - m_y = 0, \\
&\delta u_0' : a_{22}u_0'' + M_y^{\mathrm{T}} = 0, \\
&\delta v_0' : a_{33}v_0'' + M_x^{\mathrm{T}} = 0.
\end{aligned} \tag{29a–d}$$

As a mere remark, the governing equations for the shearable and unshearable beam models feature the same order, namely eight, and as a result, in both cases, four boundary conditions should be prescribed at $z = 0, L$.

It should be pointed out that when discarding the rotatory inertia terms in Eqs. (27), and in the absence of damping, these equations coincide with those from Ref. [7].

4. Solution methodology of the eigenvalue problem

Toward the goal of solving the eigenvalue problem of the gyroscopic system as given by Eqs. (24)–(26) corresponding to the shearable beam model, the following steps will be implemented. The first one consists of the representation of displacement functions in the form

$$u_0(z,t) = \mathbf{U}^{\mathrm{T}}(z)\mathbf{q}_u(t), \quad v_0(z,t) = \mathbf{V}^{\mathrm{T}}(z)\mathbf{q}_v(t),$$

$$\theta_x(z,t) = \mathbf{X}^{\mathrm{T}}(z)\mathbf{q}_x(t), \quad \theta_y(z,t) = \mathbf{Y}^{\mathrm{T}}(z)\mathbf{q}_y(t), \tag{30a–d}$$

where

$$\mathbf{U} \equiv [u_1,\ u_2,\ldots,\ u_N]^{\mathrm{T}}, \quad \mathbf{V} \equiv [v_1,\ v_2,\ldots,\ v_N]^{\mathrm{T}},$$

$$\mathbf{X} \equiv [X_1,\ X_2,\ldots,\ X_N]^{\mathrm{T}}, \quad \mathbf{Y} \equiv [Y_1,\ Y_2,\ldots,\ Y_N]^{\mathrm{T}} \tag{31a–d}$$

are the vectors of trial functions, and

$$\mathbf{q}_u \equiv [q_1^u,\ q_2^u,\ldots,\ q_N^u]^{\mathrm{T}}, \quad \mathbf{q}_v \equiv [q_1^v,\ q_2^v,\ldots,\ q_N^v]^{\mathrm{T}},$$

$$\mathbf{q}_x \equiv [q_1^X,\ q_2^X,\ldots,\ q_N^X]^{\mathrm{T}}, \quad \mathbf{q}_y \equiv [q_1^Y,\ q_2^Y,\ldots,\ q_n^Y]^{\mathrm{T}} \tag{31e–h}$$

denote the vectors of generalized co-ordinates, while the superscript T denotes the transpose operation. Replacing representation (30) in the variational integral (19) (see Ref. [8]), considered in conjunction with the proper expressions of the various energies involved in Eqs. (20)–(22) and the kinematical equations (1) and (2), and carrying out the indicated variations and the required integration, the discretized form of the equation governing the motion of the gyroscopic system is obtained as

$$\mathbf{M}\ddot{\mathbf{q}}(t) + \mathbf{G}\dot{\mathbf{q}}(t) + \mathbf{K}\mathbf{q}(t) = 0. \tag{32}$$

Herein, $\mathbf{M}$ and $\mathbf{K}$ are the symmetric mass matrix and the stiffness matrix, respectively, $\mathbf{G}$ is the skew-symmetric gyroscopic matrix, while

$$\mathbf{q}\left(\equiv \left[\mathbf{q}_u^{\mathrm{T}},\ \mathbf{q}_v^{\mathrm{T}},\ \mathbf{q}_x^{\mathrm{T}},\ \mathbf{q}_y^{\mathrm{T}}\right]^{\mathrm{T}}\right) \tag{33}$$

is the $4N \times 1$ overall vector of generalized coordinates. Using the method presented in Ref. [8], Eq. (32) will be expressed in state-space form. In this sense, upon defining the $8N \times 1$ state vector $\mathbf{X} = [\mathbf{q}^{\mathrm{T}},\ \dot{\mathbf{q}}^{\mathrm{T}}]^{\mathrm{T}}$ and adjoining the identity $\dot{\mathbf{q}} = \dot{\mathbf{q}}$, Eq. (32) is converted to

$$\dot{\mathbf{X}}(t) = \mathbf{A}\mathbf{X}(t), \tag{34}$$

where the $8N \times 8N$ state matrix $\mathbf{A}$ is given by

$$\mathbf{A} = \begin{bmatrix} \mathbf{0} & \mathbf{I} \\ -\mathbf{M}^{-1}\mathbf{K} & -\mathbf{M}^{-1}\mathbf{G} \end{bmatrix}, \tag{35}$$

while **I** and **O** are the identity and the zero matrix, respectively. Upon expressing $\mathbf{X}(t)$ in Eq. (34) as

$$\mathbf{X}(t) = \mathbf{Z}\exp(\Lambda t), \tag{36}$$

where **Z** is a constant vector and Λ a constant-valued quantity, both generally complex, a standard eigenvalue problem is obtained:

$$(\mathbf{Z} - \Lambda\mathbf{I})\mathbf{X} = 0, \tag{37}$$

that can be solved for the eigenvalues Λ_r and eigenvectors $\mathbf{X}_r$. As shown in Ref. [3], depending upon the positive definiteness, positive semi-definiteness and negative definiteness of the stiffness matrix **K** which contains elements associated with Ω^2 and the compressive load, the eigenvalues of Eq. (34) can be, respectively: (1) purely imaginary, which implies pure oscillatory motion, the eigenvalues appearing as purely imaginary pairs $\Lambda_r = \pm i\omega_r$ $(r = 1, 2, \ldots, N)$, where ω_r are the rotating (whirling) frequencies; (2) at least one eigenvalue can be zero (which implies divergent motion); or (3) the eigenvalues can be complex conjugate with at least one of these having a positive real part, which implies unstable motion, the instability being of the flutter type. Although this type of instability is typical for non-conservative systems, this can occur also in the case of conservative gyroscopic systems.

5. Validation of the solution methodology

In order to validate the solution methodology that was used here, namely the *extended Galerkin method* (EGM), a comparison of the divergence instability predictions for a circular cylindrical spinning shaft based on the present solution methodology and on the *dynamic stiffness method* (DSM) used in Ref. [9], is presented. In Ref. [9] the case of a solid beam was considered. Since the equations for solid and thin-walled beams are similar in form, the following global parameters translated to our notations were considered: $a_{44}/a_{22} = a_{55}/a_{33} = 21.82(1/m^2)$; $(b_4 + b_{14})/a_{33} = (b_5 + b_{15})/a_{22} = 3.71 \times 10^{-8}(s^2)$; $b_1/a_{44} = b_1/a_{55} = 1.09 \times 10^{-7}(s^2)$, and $L = 10(m)$.

Table 2
Comparison of the divergence critical spinning speed of the shaft based on the extended Galerkin method and dynamic stiffness method

Critical spinning speed Ω (rad/s)				
Mode number	Euler–Bernoulli beam		Timoshenko beam	
	DSM [9]	EGM	DSM [9]	EGM
1	64.01	64.01	63.92	63.88
2	256.1	256.1	254.5	254.1
3	1024.2	1024.2	568.4	565.6
4	1600.3	1600.3	999.8	995.9
5	2304.5	2304.5	1540.9	1539.5

The results of this comparison are supplied in Table 2, wherefrom the conclusion that both solutions show an excellent agreement becomes evident. Moreover, the results reveal that the Euler–Bernoulli model overestimates the critical speed, especially at the high mode number.

6. Results

Throughout the numerical simulations, unless otherwise stated, the following geometrical characteristics are used: $L = 80$ in (2.032 m), $h = 0.4$ in (0.01 m), $R = 5$ in (0.127 m).

In addition, the displayed results will be presented in terms of the normalized natural frequencies and spin rate that are defined by $\overline{\omega}_i \equiv \omega_i/\hat{\omega}_1$, $\overline{\Omega} \equiv \Omega/\hat{\omega}_1$, where the normalizing fundamental frequency $\hat{\omega}_1$ (= 375.43 rad/s) corresponds to the fully-metallic non-spinning beam counterpart, in the case of the absence of the thermal gradient ($\lambda = 0$) and of the axial load.

In Fig. 3, in the absence of the compressive load, the dependence of $\overline{\omega}_1(\equiv \omega_1/\hat{\omega}_1)$ vs. the normalized spin rate $\overline{\Omega}(\equiv \Omega/\hat{\omega}_1)$ is depicted. Two extreme values of the parameter K, corresponding to the fully metallic beam ($K = 10$) and to the fully ceramic one ($K = 0$) have been considered.

From this figure it clearly appears that for $\overline{\Omega} = 0$, due to the circular cylindrical beam shape, the frequencies in transversal and lateral bending of each mode coincide. For $\overline{\Omega} \neq 0$, due to the Coriolis gyroscopic effect, a bifurcation of natural frequencies is experienced, resulting in the upper and lower frequency branches (see e.g. Refs. [3,7,10]). The minimum spin rate at which the lowest rotating natural frequency becomes zero-valued is referred to as the critical spinning speed,

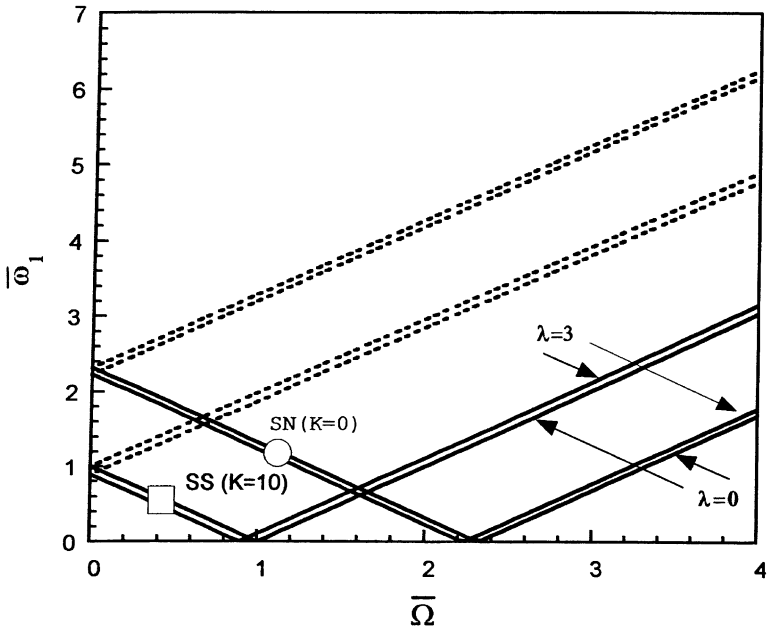

Fig. 3. The effect of temperature gradient on the spinning speed: $\overline{P} = 0$; —, lower branch; – – – –, upper branch.

and corresponds to the divergence instability. Beyond the critical spinning speed, as it appears in Fig. 3, the increase of $\overline{\Omega}$ results in the increase of the frequency corresponding to the lower frequency branch.

The displayed results also reveal that in the case of the fully metallic beams, the lowest non-rotating natural frequency and the lowest critical divergence spin speed are experienced. However, with the decay of K, implying an increase of the concentration of the ceramic phase in the detriment of the metallic one, a beneficial trend consisting both of the increase of the non-spinning natural frequencies and of the critical spinning speed are resulting. As a limiting case, for a fully ceramic beam, the highest non-rotating natural frequency and critical speed of divergence are resulting.

At the same time, for this case, the upper and lower frequency branches remain, for any $\overline{\Omega}$, parallel to each other. From this plot it appears that the thermal degradation of material properties, materialized by the thermal gradient measure λ, has rather marginal implications on the eigenfrequency and divergence spin.

In Fig. 4 is depicted the variation of the frequency $\overline{\omega}_1$ in the condition of the non-spinning beam ($\Omega = 0$), and for selected values of the volume fraction parameter K, vs. the dimensionless compressive axial load $\overline{P}(\equiv P/P_{\mathrm{cr}})$, where the critical axial compressive load $P_{\mathrm{cr}} \equiv Sa_{33}^{m}/L^2$, and $S = 2.407$, while $a_{33}^{m}(\equiv 1.359 \times 10^7\,\mathrm{N\,m^2})$ is the bending normalizing stiffness corresponding to the non-rotating fully-metallic beam for the case $\lambda = 0$.

The results reveal that the increase of the compressive load yields a continuous decrease of the fundamental non-rotating eigenfrequency. The values of $\overline{P}$ yielding the frequency to vanish constitutes the critical (buckling) axial load. The loss of stability in this case is by divergence. The results of Fig. 4 reveal that the increase of the ceramic phase in the detriment of the metallic one,

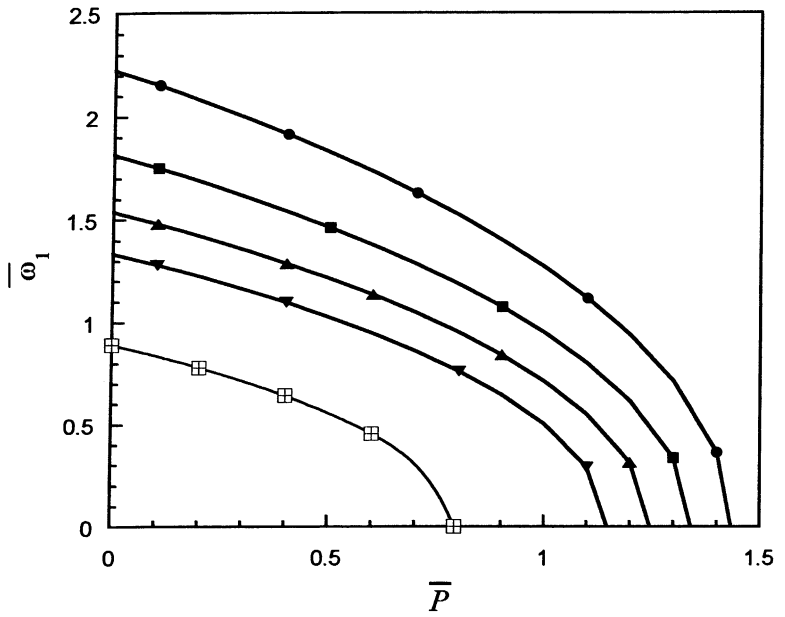

Fig. 4. Variation of the first non-rotating natural frequency vs. the dimensionless compressive axial load for selected values of K, ($\lambda = 3$, $\overline{\Omega} = 0$): —●—, SN ($K = 0$); —■—, $K = 0.2$; —▲—, $K = 0.5$; —▼—, $K = 1.0$; —⊞—, SS.

that reverts to the decrease of the parameter K, is accompanied by both an increase of the eigenfrequency and of the buckling load.

With the start of the beam spinning, a new phenomenon is experienced. In this sense, in Fig. 5, for a prescribed spin speed ($\overline{\Omega} = 0.5$), $\lambda = 3$, and selected values of K, the variation of $\overline{\omega}_1$ vs. $\overline{P}$ is depicted.

The results reveal that for a certain $\overline{P}$ that depends on the selected value of the parameter K, the upper and lower branches of the rotating frequency coalesce, and beyond that specific value of $\overline{P}$, the frequencies of the two branches become complex conjugate.

That specific value of $\overline{P}$ at which the lower and upper frequency branches are merging corresponds to the compressive load of flutter, $\overline{P}_{\text{flutter}}$ (see Refs. [11,12]). As it clearly appears from Fig. 5, the spinning circular cylindrical beam experiences also the instability by divergence $\overline{P}_{\text{div}}$ at that critical value of $\overline{P}$ where the eigenfrequency vanishes.

From Fig. 5 it is also seen that when the ceramic constituent phase increases in the deteriment of the metallic phase, both $\overline{P}_{\text{div}}$ and $\overline{P}_{\text{flutter}}$ increase. Moreover, with the decrease of K their values become closer and closer, but always we have that $\overline{P}_{\text{div}} < \overline{P}_{\text{flutter}}$.

With the increase of $\overline{\Omega}$, as Figs. 6(a) and (b) reveal, the beam whose constituent phase is richer in metal, experiences only the flutter instability. With the increase of $\overline{\Omega}$ this trend is exacerbated.

In this sense, from Fig. 6(a), one can see that for $\overline{\Omega} = 1$, only the beam constituted of full metal experiences the flutter instability, while from Fig. 6(b), when $\overline{\Omega} = 2$, only the fully ceramic beam experiences both divergence and flutter, the other ones corresponding to various K experiencing both types of instability, i.e. flutter and divergence. The trend of the increase of the $\overline{P}_{\text{flutter}}$ with the decay of K toward fully ceramic beams remains certainly valid in all these cases.

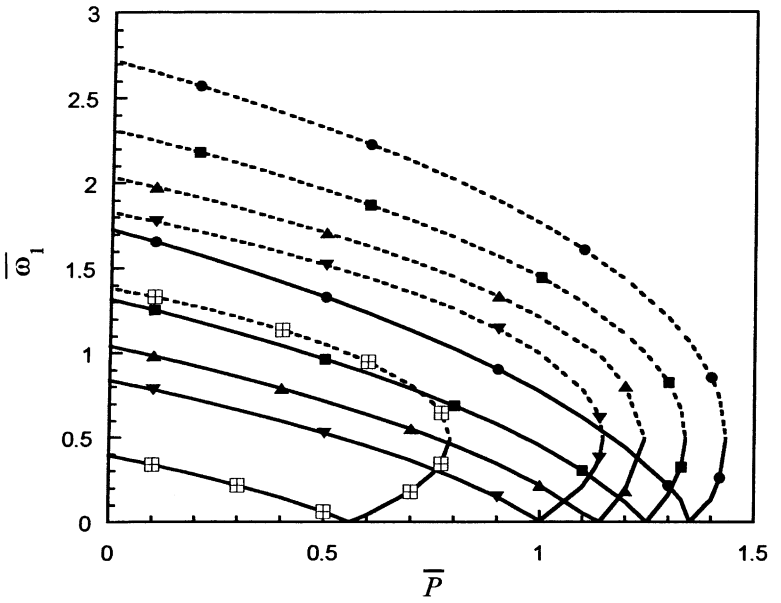

Fig. 5. Variation of the upper and lower frequency branches vs. the compressive axial load for selected values of K, ($\lambda = 3$, $\overline{\Omega} = 0.5$): —, upper branch; – – – – –, lower branch; —●—, SN ($K = 0$); —■—, $K = 0.2$; —▲—, $K = 0.5$; —▼—, $K = 1.0$; —⊞—, SS.

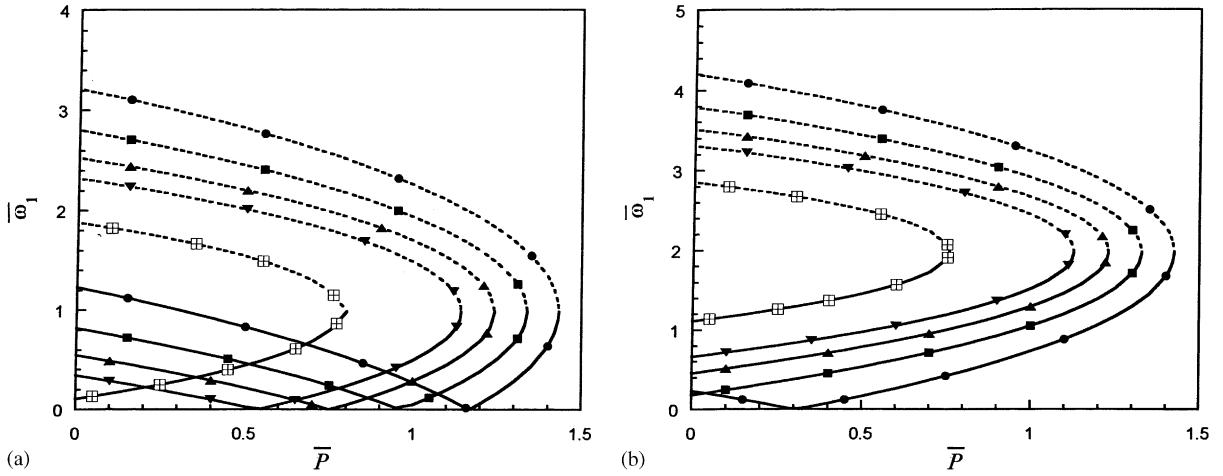

Fig. 6. Variation of the upper and lower frequency branches vs. the compressive axial load for selected values of K ($\lambda = 3$) for: (a) $\overline{\Omega} = 1$; (b) $\overline{\Omega} = 2$. —, upper branch; – – – – –, lower branch; —●—, SN ($K = 0$); —■ —, $K = 0.2$; —▲—, $K = 0.5$; —▼—, $K = 1.0$; —⊞—, SS.

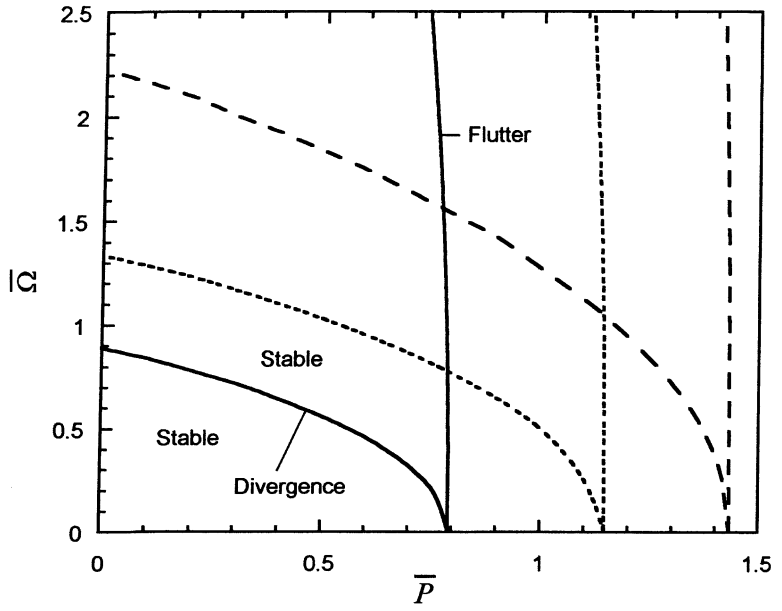

Fig. 7. Stability map in the $\overline{\Omega} - \overline{P}$ plane displaying the domains of stability, divergence and flutter instability boundaries, for selected values of K ($\lambda = 3$): ——, SS; – – – –, $K = 1.0$; — — —, SN ($K = 0$).

In Fig. 7 there is depicted a stability plot of the spinning system in the $\overline{\Omega} - \overline{P}$ plane, for a fixed beam thickness, thermal gradient $\lambda = 3$, and three selected values of K. As it can be seen, this plot summarizes the behavior, from the instability point of view, as presented in Figs. 4–6. In this plot the divergence boundary and that of flutter are indicated, as well as the stable domains.

From this plot one can see that with the increase of $\overline{\Omega}$ and/or $\overline{P}$, instabilities by divergence and flutter may occur. This figure as well as the previous ones, Figs. 4–6, reveal that for a spinning and compressed circular cylindrical beam, the divergence occurs only on the indicated boundary, that is bordered by the stability domains. Moreover, the results from Fig. 7 show that the gyroscropic effects increasing with $\overline{\Omega}$ contribute to the increase of the stability domain.

The results reveal again that the decrease of K towards the fully ceramic beam, $K = 0$, yields a dramatic increase of the stability domains and a shift of the divergence and flutter instability boundaries toward larger compressive loads. In order to have a better view of the occurrence of the instability, in Table 3 full information about the combined implications of the spinning speed, compressive load and the thermal gradient on both the instability by divergence and flutter of the spinning cylindrical beam, and on the domains of stability are presented. The conclusions emerging from this table enforce the previously outlined ones.

In Fig. 8 there is depicted the variation of $\overline{\omega}_1$ vs. K, for selected slenderness ratios L/R, where L is fixed to $L = 80$ in, and for two values of λ. The results reveal that the increase of R yields an increase of the fundamental frequency. It is also seen that the effects of the thermal degradation of material properties appear to be exacerbated in the case of larger R, and tend to be attenuated when R decreases. However, as it appears from Fig. 9 depicting the variation of the eigenfrequency $\overline{\omega}_1$ vs. K for selected values of the thickness ratio h/R, where $R = 5$ in, is fixed, and for two values of λ, the effect of the beam wall thickness is really marginal.

In Fig. 10 is depicted the variation of the non-rotating fundamental frequency $\overline{\omega}_1$ vs. K for selected values of the dimensionless compressive load and a fixed value of $\lambda(= 3)$. The results reveal that the increase of $\overline{P}$ yields a decrease of $\overline{\omega}_1$, a trend that is exacerbated by the increase of $\overline{P}$. As a general conclusion emerging from Figs. 8 to 10, the increase of K, results in a decay of the eigenfrequencies.

Table 3
Stability and instability domains as influenced by the spinning speed, compressive load, and volume fraction parameter ($0 \leqslant \overline{P}_{\text{stable}} < \overline{P}_{\text{div}}, \overline{P}_{\text{div}} \leqslant \overline{P}_{\text{stable}} < \overline{P}_{\text{flutter}}$)

	$\overline{\Omega}$	0		0.5		1.0		1.5		2.0	
		$\lambda = 0$	$\lambda = 3$	$\lambda = 0$	$\lambda = 3$	$\lambda = 0$	$\lambda = 3$	$\lambda = 0$	$\lambda = 3$	$\lambda = 0$	$\lambda = 3$
$K = 0$	$\overline{P}_{\text{div}}$	1.553	1.434	1.488	1.350	1.289	1.170	0.943	0.823	0.432	0.307
(SN)	$\overline{P}_{\text{flutter}}$	*	*	1.552	1.434	1.550	1.433	1.546	1.429	1.542	1.425
$K = 0.2$	$\overline{P}_{\text{div}}$	1.461	1.341	1.369	1.249	1.078	0.965	0.579	0.460	*	*
	$\overline{P}_{\text{flutter}}$	*	*	1.460	1.340	1.457	1.339	1.452	1.333	1.446	1.328
$K = 0.5$	$\overline{P}_{\text{div}}$	1.369	1.247	1.250	1.128	0.879	0.745	0.212	0.079	*	*
	$\overline{P}_{\text{flutter}}$	*	*	1.368	1.245	1.368	1.243	1.358	1.237	1.349	1.229
$K = 1.0$	$\overline{P}_{\text{div}}$	1.278	1.148	1.131	1.000	0.670	0.537	*	*	*	*
	$\overline{P}_{\text{flutter}}$	*	*	1.276	1.148	1.271	1.143	1.263	1.137	1.253	1.127
SS	$\overline{P}_{\text{div}}$	1.000	0.792	0.770	0.562	0.009	*	*	*	*	*
	$\overline{P}_{\text{flutter}}$	*	*	0.997	0.791	0.991	0.785	0.979	0.772	0.964	0.758

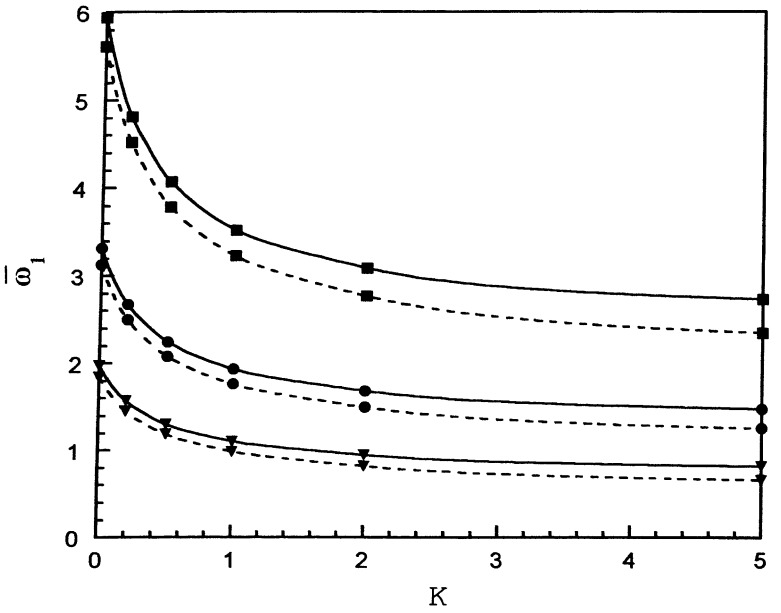

Fig. 8. Variation of the fundamental natural frequency against K for selected values of L/R and two values of λ: ——, $\lambda = 0$; - - - - - , $\lambda = 4$ ($\overline{\Omega} = \overline{P} = 0.2, L =$ fixed $= 80$ in). —▼—, $L/R = 16$; —●—, $L/R = 10$; —■—, $L/R = 5$.

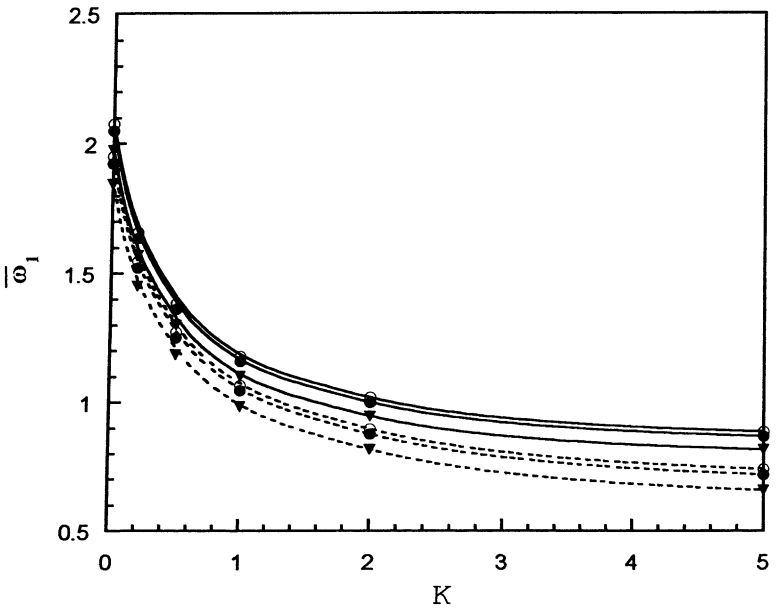

Fig. 9. Variation of the fundamental natural frequency against K for selected values of h/R and two values of λ: ——, $\lambda = 0$; - - - - - , $\lambda = 4$ ($\overline{\Omega} = P = 0.2; R = 5$ in). —▼—, $h/R = \frac{4}{50}$; —●—, $h/R = \frac{8}{50}$; —○—, $h/R = \frac{12}{50}$.

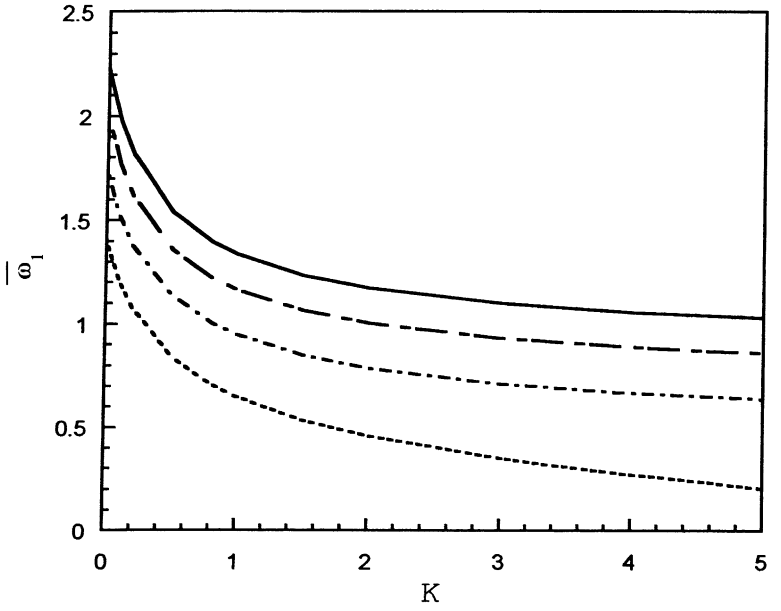

Fig. 10. Fundamental non-rotating natural frequency vs. the parameter K for selected values of the axial load: ——, $\overline{P}=0$; – ———, $\bar{P}=0.3$; —·—·—, $\overline{P}=0.6$; – – – –, $\overline{P}=0.9$.

Table 4
Comparison of dimensionless first natural frequency $\overline{\omega}_1$ determined via the simple rule of mixtures (R-M) and the Mori–Tanaka (M-T) scheme for selected values of the temperature gradient and the volume fraction parameter ($\overline{\Omega}=0, \overline{P}=0$)

	$\lambda=0$		$\lambda=3$		$\lambda=5$	
	R-M	M-T	M-R	M-T	M-R	M-T
$K=0$ (SN)	2.3145	2.3145	2.2249	2.2249	2.1526	2.1526
$K=0.2$	1.8920	1.8830	1.8132	1.8010	1.7417	1.7100
$K=0.5$	1.6127	1.6010	1.5392	1.5233	1.4635	1.4253
$K=1.0$	1.4075	1.3967	1.3354	1.3206	1.2502	1.2408
SS	1.0000	1.0000	0.8903	0.8903	0.6792	0.6792

Finally, in Table 4 is presented a comparison of the first dimensionless natural frequency $\overline{\omega}_1$ determined for selected values of λ and K, via the simple rule of mixture (R-M) and the Mori–Tanaka (M-T) scheme [6], for ($\overline{\Omega}=0, \overline{P}=0$).The results based on these two homogeneization methodologies reveal an excellent agreement of predictions.

7. Conclusions

A study devoted to the vibrational and stability behavior of FGM spinning circular cylindrical thin-walled beams was presented, and the implications played by the conservative and gyroscopic

forces on their instability behavior have been highlighted. In addition, the effects played by the presence of the two phases in the constitution of the FGM, i.e. ceramic and metal, and the relative proportion of these phases measured in terms of the power-law parameter K have been addressed. The thermal degradation of the material characteristics has been included in the structural model and its effects have been assessed. As shown, at the conditions described in the paper, the spinning beam can experience instabilities by flutter and divergence and in this context, the strong effect played by the volume fraction parameter was outlined. As revealed in Ref. [7], incorporation of structural damping can have a strong influence on the stability of a spinning shaft, as compared to the case of its discard. Its effect will be addressed in a forthcoming paper.

It is hoped that the results and conclusions reported here will be of benefit to those engaged in the study, design and implementation of the FGM concept in spinning circular cylindrical structures.

Appendix A. Expressions of stiffness, mass and temperature terms

The 1-D thermal loading terms are expressed by

$$M_x^{\mathrm{T}}(z) = \oint \left[y\hat{N}_{zz}^{\mathrm{T}} - \frac{\mathrm{d}x}{\mathrm{d}s}\hat{L}_{zz}^{\mathrm{T}} \right] \mathrm{d}s, \quad M_y^{\mathrm{T}}(z) = \oint \left[x\hat{N}_{zz}^{\mathrm{T}} + \frac{\mathrm{d}y}{\mathrm{d}s}\hat{L}_{zz}^{\mathrm{T}} \right] \mathrm{d}s,$$

where

$$\hat{N}_{zz}^{\mathrm{T}}(s,z) = \left(1 - \frac{A_{12}}{A_{11}}\right) N_{zz}^{\mathrm{T}}; \quad \hat{L}_{zz}^{\mathrm{T}} = L_{zz}^{\mathrm{T}} - \frac{B_{12}}{A_{11}} N_{zz}^{\mathrm{T}}$$

and

$$\left(N_{zz}^{\mathrm{T}}, L_{zz}^{\mathrm{T}}\right) = \int_{-h/2}^{h/2} \Delta T \hat{\alpha}(Q_{11} + Q_{12})(1, n)\, \mathrm{d}n,$$

A_{ij} and B_{ij} denoting the shell-stiffnesses in stretching and coupled bending–stretching, respectively. Concerning the non-vanishing stiffness and inertia coefficients, these are

$$a_{22} = a_{33} = \pi R[K_{11}R^2 + K_{44}], \quad a_{44} = a_{55} = \pi R[K_{22} + A_{44}],$$
$$b_4 + \delta_n b_{14} = b_5 + \delta_n b_{15} = \pi R[m_0 R^2 + \delta_n m_2].$$

In these expressions [4],

$$K_{11} = A_{11} - \frac{A_{12}^2}{A_{11}}; \quad K_{22} = A_{66}; \quad K_{44} = D_{22} - \frac{B_{12}^2}{A_{11}}$$

and

$$(m_0; m_2) = \int_{-h/2}^{h/2} \left[(\rho_c - \rho_m) \left(\frac{2n+h}{2h}\right)^K (1; n^2) + \rho_m (1; n^2) \right] \mathrm{d}n.$$

References

[1] S.Y. Oh, L. Librescu, O. Song, Thermoelastic modeling and vibration of functionally graded thin walled rotating blades, *AIAA Journal* 41 (10) (2003) 2051–2060.
[2] O. Song, L. Librescu, Anisotropy and structural coupling on vibration and instability of spinning thin-walled beams, *Journal of Sound and Vibration* 204 (3) (1998) 477–494.
[3] O. Song, N.H. Jeong, L. Librescu, Implications of conservative and gyroscopic forces on vibration and stability of elastically tailored rotating shaft modeled as composite thin-walled beams, *Journal of the Acoustical Society of America* 109. 972–981.
[4] O. Song, L. Librescu, Free vibration of anisotropic composite thin-walled beams of closed cross-section contour, *Journal of Sound and Vibration* 167 (1) (1993) 129–147.
[5] J.N. Reddy, C.D. Chin, Thermomechanical analysis of functionally graded cylinders and plates, *Journal of Thermal Stresses* 21 (1998) 593–626.
[6] Z.-W. Cheng, R.C. Batra, Three dimensional thermoelastic deformation of a functionally graded elliptic plate, *Composites, Part B* 31 (2) (2000) 97–106.
[7] M.B. Rosales, C.P. Filipich, Dynamic stability of a spinning beam carrying an axial dead load, *Journal of Sound and Vibration* 163 (2) (1993) 283–294.
[8] L. Librescu, L. Meirovitch, S.S. Na, Control of cantilevers vibration via structural tailoring and adaptive materials, *AIAA Journal* 35 (8) (1997) 1309–1315.
[9] G. Curti, F.A. Raffa, F. Vatta, An analytical approach to the dynamic of rotating shafts, *Meccanica* 27 (1992) 285–292.
[10] C.P. Filipich, M.J. Maurizi, M.B. Rosales, Free vibration of a spinning uniform beam, with ends elastically restrained against rotation, *Journal of Sound Vibration* 116 (1987) 475–482.
[11] K. Huseyin, R.H. Plaut, Transverse vibrations and stability of systems with gyroscopic forces, *Journal of Structural Mechanics* 3 (2) (1974–1975) 163–177.
[12] D.M. Ku, L.W. Chen, Stability and whirl speeds of rotating shaft under axial loads, *International Journal of Analytical and Experimental Model Analysis* 9 (2) (1994) 111–123.